Inclusive neutron production by 337 MeV/nucleon neon ions on carbon, aluminum, copper, and uranium

R. A. Cecil, B. D. Anderson, A. R. Baldwin, and R. Madey
Department of Physics, Kent State University, Kent, Ohio 44242

W. Schimmerling, J. W. Kast,* and D. Ortendahl†
Lawrence Berkeley Laboratory, Berkeley, California 94720
(Received 4 May 1981)

We measured inclusive double-differential cross sections at angles of 30, 45, 60, and 90 deg for the production of neutrons above about 12 MeV from 337 MeV/nucleon neon ions bombarding targets of C, Al, Cu, and U. Three different energy regions can be distinguished in the neutron spectra: (1) a low-energy "evaporation" region, (2) a high-energy exponential tail reflecting the internal momentum distribution of the nucleons, and (3) an intermediate energy region reflecting quasifree and preequilibrium processes. The intermediate-energy region becomes less pronounced with increasing angle and is almost nonexistent at 90 deg. This behavior is consistent with the interpretation that the intermediate-energy region consists mainly of scattering processes with a few direct collisions. The intermediate-energy region is relatively flat at the forward angles and merges into an exponential falloff at wide angles. The 30-deg spectrum from the carbon target shows a broad peak around 150 MeV, which we interpret as a signature of quasifree nucleon-nucleon collisions. Although the neutron detection threshold does not permit us to see the evaporation peaks, we do see evidence of the evaporation tails. The evaporation yields apparent in our spectra increase with the mass number of the target. The neutron spectra differ from proton spectra reported for similar targets at 385 and 393 MeV/nucleon. The neutron-to-proton cross section ratios are fit well by an intranuclear-cascade model calculation, but poorly by a "firestreak" model calculation.

[NUCLEAR REACTIONS C, Al, Cu, U(Ne, nX), $E=337$ MeV/nucleon. Measured double-differential cross sections at $\theta_{lab}=$ 30, 45, 60, and 90 deg. Deduced total integrated neutron cross sections above 25 MeV. Compared neutron spectra with proton spectra and neutron/proton cross section ratios with the firestreak model.]

I. INTRODUCTION

New states of nuclear matter such as pion condensates or density isomers[1] may be achieved in relativistic heavy-ion reactions. In order to recognize the signatures of new phenomena, it is helpful to understand the systematics of relativistic heavy-ion reactions. Several studies[2–5] of the emitted proton and composite-particle cross sections were performed to determine these systematics. The observed composite-particle spectra appear to be described well by a coalescence model[6] of final-state interactions. Model calculations used the measured proton cross sections and assumed that the neutron cross sections would simply scale by the neutron-to-proton ratio of the target plus projectile. Our earlier measurements[7] of neutron cross sections from neon on uranium revealed that the assumed scaling of the neutron cross sections is inadequate.

Several theoretical models attempt[8–13] to describe the available experimental measurements of nucleon spectra from relativistic heavy-ion reactions. These theoretical descriptions include thermodynamic models such as the fireball[8] and the firestreak[9,10] models; hydrodynamic models such as those of Amsden *et al.*[11,12] and intranuclear-

cascade models such as those of Yariv and Fraenkel,[13] Bondorf *et al.*,[14] and Stevenson.[15] None of these models has been shown to provide consistent agreement with the experimental measurements over a reasonable range of projectile-target combinations, beam energies, and scattering angles.

We report here inclusive doubly differential cross sections for neutrons above 12 MeV at angles of 30, 45, 60, and 90 deg produced in targets of carbon, aluminum, copper, and uranium by 337 MeV/nucleon neon ions from the Bevalac accelerator of the Lawrence Berkeley Laboratory. Taken together with the available data for emission of protons and light nuclei, our results provide constraints on physical assumptions underlying various models. Schimmerling *et al.*[7] showed that the ratio of the neutron-to-proton (n/p) cross sections from uranium cannot be explained satisfactorily by the firestreak model. Gyulassy and Kauffman[16] suggested that Coulomb effects in the final state of the emitted proton may account for part of the difference in the neutron and proton cross sections; however, Stevenson[17] used an intranuclear cascade model to conclude that the observed energy dependence of the n/p ratio may be explained by differences in the beam energies of the proton and neutron measurements. Stevenson accounts for neutrons that are carried away by composite particles and reproduces the experimental n/p ratios for uranium within the accuracy of the measurements. The measurements reported here extend our earlier results by providing new targets for further comparisons. The low mass number targets provide better possibilities for observing signatures of quasifree scattering contributions in these reactions.

II. EXPERIMENTAL PROCEDURE

The energy of a neutron produced in the target was determined by the time-of-flight (TOF) technique. We measured the time difference between the detection of a neon ion in a scintillator beam telescope and the detection of a neutron in one of four counters located 3—6 m from the target. The neutron energy was calculated from the TOF of the neutron measured relative to the observed prompt gamma peak in each TOF spectrum. Absolute neutron cross sections were obtained by counting the number of neon ions which passed through the beam telescope. The neutron detection efficiency of each neutron counter was calculated with the computer code of Cecil *et al.*[18] for specified pulse-height thresholds.

A. Experimental arrangement

A scale drawing of the experimental arrangement is shown in Fig. 1. After emerging from the vacuum line, the beam was incident on a 7.5-cm square by 0.8-mm thick NE-102 plastic scintillation counter $S2$, the target T, and then proceeded to a reentrant beam dump. Incident beam ions were detected by a beam telescope consisting of scintillation counters $S1$ and $S2$ in coincidence. Detector $S1$ was positioned 10 m upstream of the target. The $S1$ counter was a 20-cm square by 0.63-cm thick Pilot B plastic scintillator with two 1-m long tapered Lucite [trade name of the DuPont Co. for an acrylic (methyl methacrylate) resin with composition $(C_5H_8O_2)_n$ and density 1.18 g/cm^3] light pipes mounted on opposite edges. A 56AVP photomultiplier tube (PMT) with a high counting-rate PMT base[19] was mounted on the end of each light pipe.

The beam in the experimental area was tuned with the aid of wire chambers placed at the target position and at the entrance to the beam dump. The wire chambers were removed during the data-taking runs. The beam transport system produced an approximately parallel beam with a spot size at the target of about 4 cm vertically by 5 cm horizontally. About 20% of the beam through $S1$ did not pass through $S2$ and contributed to the observed background. Two scintillation counters DR

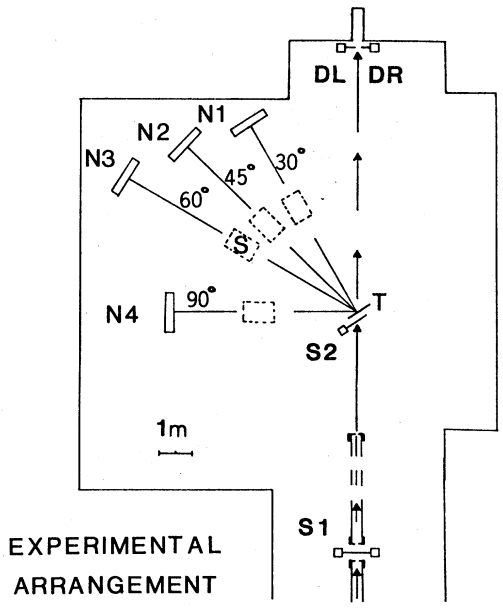

FIG. 1. Experimental arrangement.

and *DL* were placed at the edges of the beam dump to monitor the position of the beam during the experiment. Typically, less than 2% of the beam was detected by the *DR* and *DL* counters.

The neon-ion beam extracted from the Bevalac had an energy of 407 MeV/nucleon with an uncertainty of 1−2 %. The beam was delivered at a rate of 15 macropulses per min. In the extraction mode with the radio frequency on, each macropulse was about one second long with a 562 ns microstructure. The beam incident on the target had an energy of 369 MeV/nucleon which was determined by a calculation of the energy loss in the materials in the beam line. The number of neon ions incident on the target per macropulse was typically about 2×10^5 with variations from about 5×10^4 to 5×10^5.

Target thicknesses were selected to provide about 20% beam-energy loss. Each of the five targets was 10 cm square and was supported in the beam by two 25.4-μm Mylar [trade name of the DuPont Co. for a polyester film with composition $(C_{10}H_8O_4)_n$ and density 1.4 g/cm^3] sheets suspended from an aluminum frame. The targets were oriented at an angle of 45 deg to the beam to minimize the path length in the target of the detected neutrons. The carbon, aluminum, copper, and depleted ^{238}U targets were 3.06 ± 0.04, 3.38 ± 0.04, 3.81 ± 0.04, and 5.60 ± 0.06 g/cm^2 thick, respectively. Target thickness effects such as neutron attenuation and neutron production by secondary charged particles were investigated with a thin 1.86 ± 0.02 g/cm^2 depleted ^{238}U target, as discussed in Sec. III E.

Neutrons were detected in scintillators *N*1 through *N*4 positioned at angles of 30, 45, 60, and 90 deg with neutron flight paths of 5.05, 5.60, 6.04, and 4.17 m, respectively. The flight paths were measured from the center of the target to the center of each neutron counter. The active region of each detector consisted of an NE-102 plastic scintillator 1.02-m long by 10.2-cm thick; *N*1 and *N*2 were 12.7-cm high, and *N*3 and *N*4 were 25.4-cm high. A 12.5-cm diameter 58AVP PMT was coupled to each end of each scintillator by means of a tapered Lucite light pipe. Adjacent neutron detectors were placed slightly above and below the beam height to avoid the shadowing of one counter by another. Each neutron detector had a 0.63-cm thick NE-102 plastic scintillator placed in front of it to detect charged particles.

In order to determine backgrounds, separate experimental measurements were made with and without the shadow shields *S* (shown in Fig. 1) for each target and for a 50-μm Mylar (or "dummy") target. The shadow shields were 91.5-cm thick by 60-cm wide assemblies of lead bricks placed halfway between the target and a neutron detector during some experimental runs. A 12.5-cm high shadow shield was placed at either 30 or 45 deg and a 25-cm high shadow shield was placed at either 60 or 90 deg. The 91.5 cm thickness of the shadow shields is more than 5.3 attenuation lengths[20] for the highest energy neutrons measured in this experiment, which results in an attenuation factor greater than 100. Neutron scattering by a shadow shield into an adjacent (unshadowed) neutron detector was investigated by comparing experimental runs with and without one shadow shield in place. Since no additional neutron yield was observed in any of the unshadowed detectors, two detectors (e.g., 30 and 60 deg or 45 and 90 deg) were shadowed simultaneously thereafter.

B. Electronics

A simplified schematic diagram of the electronics is shown in Fig. 2. Timing signals from the beam telescope and each of the neutron detectors were obtained by the mean-timing technique.[21] The beam-telescope timing signal started a 2048

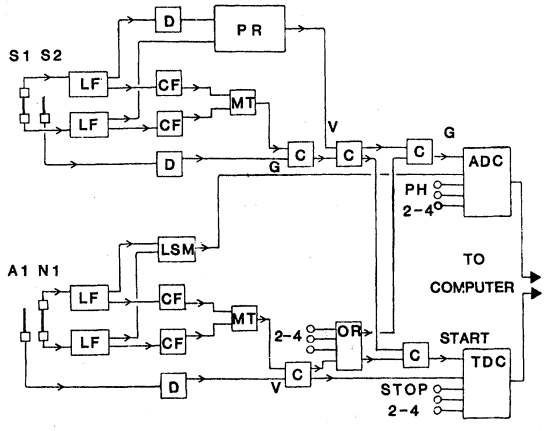

FIG. 2. Simplified electronics diagram. Key to abbreviations: LF = linear fanout module; *D*= leading edge discriminator; CF = constant fraction discriminator; LSM = linear summing module; MT = mean timer; PR = pileup rejection circuit; *C* = coincidence module; *G* = gating signal; *V* = veto input; OR = logical "or" module; ADC = CAMAC analog-to-digital converter; PH = pulse height; and TDC = CAMAC time-to-digital converter.

channel CAMAC time-to-digital converter (TDC). The neutron timing signal from each neutron detector stopped a separate channel of the TDC to produce the neutron TOF spectra. The computer data-acquisition system was triggered to accept a neutron event by the coincidence of a beam-telescope timing signal and a neutron detector timing signal. This trigger insured that no neutron events were recorded which were not coincident with the passage of a neon ion through the beam telescope. Neutron pulse-height information was obtained by summing the anode signals from the opposite ends of each neutron detector. The summed anode signals from each neutron detector went to separate inputs of a 1024 channel CAMAC analog-to-digital converter (ADC).

Pulse-height, TOF, scaler information, and a detector identification tag were recorded for each event with a PDP 11/34 computer on a temporary disc file. To monitor the operation of the detectors and to provide preliminary results, TOF and pulse-height histograms were accumulated by the computer system during data acquisition and displayed on a graphics terminal. Data were written onto magnetic tape for later off-line analysis.

An unambiguous determination of each neutron flight time required that beam ions incident on the target be separated by a minimum of 200 ns. Beam ions which occurred at intervals of less than 200 ns were eliminated by a beam pileup rejection (PR) module.[22] The PR module, which used a timing signal and an anode signal from the $S1$ detector, consists of a pulse-counting circuit and an anode-signal charge-integration circuit. A beam event was rejected if two or more particles were counted within 200 ns, or if a discrimination threshold set on the integrated anode signal was exceeded. A discrimination threshold of approximately 1.5 times the signal produced by a single beam ion was used to reject multiple particles which occurred during the dead time of the counting circuit. Emitter-follower photomultiplier tube bases[19] allowed beam counting rates greater than 5×10^5 ions per spill. The beam flux was adjusted to maximize the "good" (i.e., unpiled-up) beam. Typically, about 40% of the incident beam flux was rejected by the pileup circuit.

The anode signals from the photomultiplier tubes mounted on each end of the neutron detectors went to separate constant-fraction-timing discriminators (CF), which provided timing signals to a separate mean-timing (MT) circuit[21] for each counter. The circuit consists of an analog comparator which determines the mean arrival time of the fast logic signals from the opposite ends of a detector. A fast-timing signal is produced which is independent of the position of interaction of a detected particle along the length of a counter. The mean-timing technique provided timing resolutions of $\sim$450 ps between each of the 1-m long neutron detectors and the $S1$ scintillator of the beam telescope.

III. DATA ANALYSIS

The event-by-event list of pulse-height and TOF data recorded on magnetic tape was analyzed independently at Kent State University and at the Lawrence Berkeley Laboratory. Since pulse-height information was recorded for each TOF event, the data could be analyzed at any desired pulse-height threshold above the hardware threshold, which was set by the constant-fraction-timing discriminators for each neutron detector. Backgrounds measured with the lead shadow shields were subtracted as described in Sec. III A below. The data were compared at two different pulse-height thresholds as a check on the self-consistency of the data and the analysis procedure as described below. The resulting background-subtracted TOF spectra were converted to energy spectra and scaled by the neutron counter detection efficiencies to obtain the cross sections reported here.

A. Background subtraction

In order to determine target-induced and room-scattered backgrounds, separate experimental measurements were made with and without the shadow shields for each target and for the dummy target. The target-in spectra and the dummy-target spectra measured without shadow shields are designated as T and D, respectively. The target-in and dummy-target spectra measured with shadow shields are designated as T^* and D^*, respectively. The neutron TOF spectra (N) were determined from

$$N=(T-D)-(T^*-D^*)\,, \tag{1}$$

where the T, D, T^*, and D^* spectra are normalized to the same number of incident beam particles. Typical T, T^*, D, and D^* spectra from a uranium target are shown in Figs. 3(a)–3(d), respectively, for the counter at 30 deg. The N spectra represent

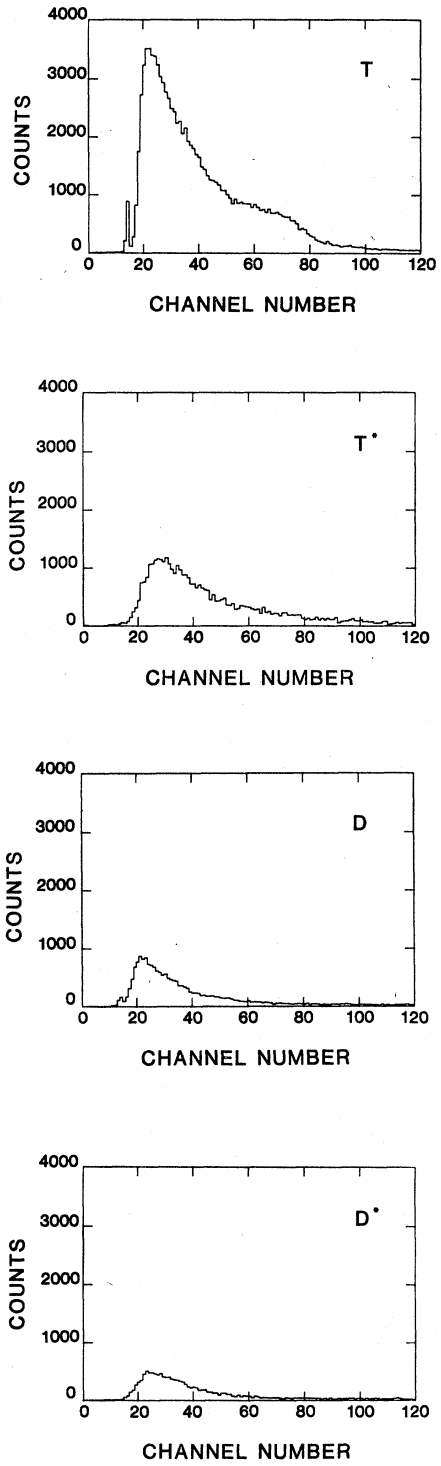

FIG. 3. Normalized time-of-flight spectra at 30 deg for (a) T, the uranium target; (b) T^*, the uranium target with a shadow shield; (c) D, the dummy target; and (d) D^*, the dummy target with a shadow shield.

neutrons from the target after subtracting backgrounds. Each of the four component spectra contain cosmic rays and other essentially time-independent backgrounds. Since each good beam particle gated the counting system on for the same period of time, the normalized component spectra contain statistically equal contributions from time-independent backgrounds. Thus, within statistics, all time-independent backgrounds cancel out in Eq. (1). In Eq. (1), time-dependent backgrounds, such as target-induced and room-scattered neutrons and gamma rays, are also removed algebraically from the N spectra. The T, T^*, D, and D^* spectra contain different contributions from the time-dependent backgrounds. The T spectra include neutrons from the target and all forms of background. The T^* spectra include room-scattered neutrons produced by the target and all other backgrounds. The D spectra consist of the neutrons produced by extraneous materials in the beam such as the Mylar target support, the beam telescope, and the air. The D^* spectra include the room-scattered neutron production by the extraneous materials in the beam.

The relative magnitudes of the four types of TOF spectra were about the same for each of the targets and did not change significantly as a function of angle. The T^* spectra were typically 50% of the T spectra below 100 MeV and decreased to about 10% of the T spectra at the highest energies measured. The D and D^* spectra varied from about 10–25% of the T spectra. The D spectra varied from about 35% of the T^* spectra below 200 MeV to only slightly less than the T^* spectra above 400 MeV. The D^* spectra varied from about 25–50 % of the T^* spectra.

For each of the N spectra, the average background level was zero for both the long flight-time region below the pulse-height threshold and the unphysical region preceding the prompt gamma peak. Since only room-scattered neutrons and time-independent backgrounds occur in these two TOF regions, the observed zero-average background indicates that there was no residual background in the N spectra. The T, T^*, D, and D^* TOF spectra were analyzed at two pulse-height thresholds as described in Sec. III B. The T^*, D, and D^* spectra were observed to decrease in magnitude relative to the T spectra at the higher pulse-height threshold.

B. Pulse-height thresholds

Before and after the experiment and at least once each day during the measurements, the pulse-

TABLE I. Double-differential cross sections for the production of neutrons at laboratory angles of 30, 45, 60, and 90 deg by 337 MeV/nucleon neon ions on carbon, aluminum, copper, and uranium.

Energy (MeV)		Neutron double-differential cross sections (mb/sr MeV)							
		carbon		aluminum		copper		uranium[a]	
T	δT	$\sigma(\theta,T)$	$\delta\sigma$	$\sigma(\theta T)$	$\delta\sigma$	$\sigma(\theta,T)$	$\delta\sigma$	$\sigma(\theta,T)$	$\delta\sigma$
					30 deg				
15.6	0.1	3.11	0.23	7.18	0.57	20.8	1.3	134	3.8
23.8	0.1	2.51	0.20	5.71	0.49	17.0	1.1	87.7	2.9
36.3	0.2	2.36	0.14	4.53	0.34	14.1	0.75	54.6	1.9
55.5	0.4	2.02	0.10	4.52	0.24	11.7	0.54	41.2	1.3
85.9	0.6	2.27	0.087	4.47	0.20	10.9	0.44	32.4	1.0
136.2	1.2	2.46	0.066	4.30	0.14	9.41	0.31	25.8	0.72
180.3	1.9	2.23	0.093	3.64	0.19	7.86	0.43	19.8	0.92
207.3	2.3	2.23	0.082	3.53	0.16	6.57	0.35	17.1	0.76
240.7	2.9	1.72	0.063	2.77	0.12	5.70	0.27	13.0	0.57
282.4	3.7	1.38	0.050	2.35	0.098	4.42	0.20	10.2	0.42
336.4	4.9	0.889	0.034	1.41	0.065	2.86	0.13	6.27	0.28
407.7	6.6	0.415	0.019	0.766	0.040	1.27	0.08	2.87	0.16
507.6	9.5	0.157	0.010	0.254	0.020	0.557	0.043	0.855	0.083
655.6	15.1	0.028	0.004	0.064	0.009	0.108	0.019	0.222	0.040
					45 deg				
14.7	0.1	2.65	0.30	3.91	0.66	16.8	1.5	136	4.3
21.8	0.1	2.28	0.26	3.83	0.54	12.5	1.2	83.0	3.3
32.1	0.2	1.88	0.19	3.58	0.38	9.20	0.86	58.6	2.2
47.4	0.3	1.61	0.13	3.55	0.26	7.72	0.57	39.1	1.4
70.5	0.5	1.57	0.096	3.21	0.19	7.35	0.43	30.0	1.0
106.6	0.8	1.64	0.068	2.78	0.14	6.78	0.30	21.9	0.74
165.9	1.4	1.19	0.042	2.04	0.088	4.25	0.17	12.3	0.43
217.7	2.3	0.824	0.047	1.25	0.10	2.86	0.20	7.57	0.48
250.6	2.8	0.500	0.035	0.918	0.074	1.94	0.15	5.83	0.35
291.1	3.6	0.313	0.025	0.562	0.055	1.34	0.11	3.55	0.24
342.6	4.6	0.169	0.015	0.261	0.034	0.571	0.068	1.70	0.15
409.1	6.1	0.065	0.010	0.091	0.022	0.272	0.044	0.664	0.093
499.6	8.5	0.023	0.005	0.040	0.012				
					60 deg				
14.2	0.1	1.96	0.21	3.95	0.45	12.3	1.0	121	3.0
20.5	0.1	2.05	0.17	3.76	0.35	11.1	0.80	74.8	2.3
29.5	0.1	1.54	0.13	2.95	0.26	8.85	0.61	52.2	1.6
42.5	0.2	1.44	0.084	2.83	0.17	7.25	0.38	36.0	1.0
61.4	0.4	1.11	0.058	2.14	0.12	5.48	0.27	24.1	0.72
89.6	0.6	1.03	0.045	1.96	0.095	4.80	0.20	17.5	0.53
133.6	1.0	0.647	0.029	1.14	0.063	2.98	0.13	10.8	0.32
170.0	1.5	0.397	0.033	0.646	0.077	1.82	0.16	5.86	0.40
190.7	1.7	0.292	0.026	0.562	0.061	1.33	0.12	4.23	0.30
215.0	2.0	0.175	0.023	0.317	0.047	0.866	0.098	3.13	0.23
244.0	2.5	0.109	0.016	0.191	0.035	0.540	0.072	1.64	0.18
280.1	3.0	0.073	0.012	0.158	0.026	0.395	0.054	1.45	0.12
324.7	3.9	0.034	0.008			0.135	0.038	0.617	0.095
381.2	5.0								
454.2	6.6								

TABLE I. (*Continued.*)

Energy (MeV)		Neutron double-differential cross sections (mb/sr MeV)							
		carbon		aluminum		copper		uranium[a]	
T	δT	$\sigma(\theta,T)$	$\delta\sigma$	$\sigma(\theta T)$	$\delta\sigma$	$\sigma(\theta,T)$	$\delta\sigma$	$\sigma(\theta,T)$	$\delta\sigma$
					90 deg				
17.5	0.1	1.18	0.064	2.65	0.16	10.1	0.39	70.6	1.1
28.6	0.2	0.730	0.047	1.77	0.11	5.83	0.26	33.3	0.66
46.9	0.4	0.510	0.022	1.19	0.054	3.52	0.13	17.5	0.33
77.7	0.7	0.266	0.013	0.653	0.033	2.03	0.080	8.43	0.20
132.2	1.4	0.072	0.006	0.193	0.016	0.620	0.038	2.60	0.090
181.9	2.4					0.184	0.034	0.698	0.075
214.6	3.0					0.080	0.024	0.272	0.050
256.9	4.0							0.126	0.032

[a]The uranium cross sections presented here are the same as those published earlier even though the energy binning is different.

height of each neutron counter was calibrated with a ^{228}Th radioactive gamma source ($E_\gamma = 2.62$ MeV). The Compton peak in the gamma-ray spectrum was taken as the calibration point and was associated with an equivalent-electron (ee) energy of 0.95 of the maximum Compton energy.[23] To calibrate the ADC's for large pulse heights, two fast linear amplifiers with measured gains of 10.0 and precision attenuators were used to obtain known multiples of the amplitude of the anode signals produced by each of the neutron counters. Since pulse-height information was recorded for each TOF event, the calibrations allowed the data to be analyzed off line at different pulse-height thresholds.

The cross sections calculated as described in Sec. III D with pulse-height thresholds of 4 and 8 MeV ee were found to be the same within the statistical uncertainties $\delta\sigma$ listed in Table I. The agreement of the high and low threshold analyses indicates that any systematic uncertainties in the pulse-height calibrations are smaller than the statistical uncertainties. Furthermore, since the higher threshold is expected to reduce potential background from nuclear gamma rays, this agreement of the analyses with different thresholds indicates also that the background subtractions are reliable. The 4 MeV ee threshold is the lowest reliable threshold energy above the hardware threshold of about 2 MeV ee. The 4 MeV ee threshold was consistent with the higher threshold analyses and was adopted for the cross sections reported here.

C. Energy resolutions

For measurements of neutron energies by the TOF method, the fractional energy resolution $\Delta T/T$ is given by the expression

$$\frac{\Delta T}{T} = \gamma(\gamma+1)\left[\frac{\Delta t}{t}\right], \tag{2}$$

with

$$\gamma = 1+\frac{T}{M}. \tag{3}$$

Here, T is the neutron kinetic energy, M is the neutron rest mass, Δt is the overall time resolution, and t is the neutron flight time. The sources contributing to Δt are (1) the intrinsic time resolutions of the neutron detectors, (2) the intrinsic time resolution of the beam telescope, (3) the time spread in the production of neutrons arising from the finite target thickness, (4) the time dispersion arising from the incident beam energy spread, and (5) the time spread resulting from the finite thickness of the neutron detectors. The means of these five time uncertainties are not all normally distributed and must be numerically convoluted. The uncertainties (3) and (4) are negligible for this experiment. Thus, for ease of computation, we approximated Δt as

$$\Delta t = [(\Delta\tau)^2+(\Delta x/v)^2]^{1/2}, \tag{4}$$

where $\Delta\tau$ is the combined time dispersion of the neutron detector and the beam telescope, Δx is the effective thickness of the neutron detector, and v is the velocity of the neutron. The assumption in Eq. (4) that the time spread resulting from the detector thickness is a Gaussian distribution with a full-

width at half-maximum (FWHM) equal to Δx overestimates the actual Δt. The combined time dispersion $\Delta\tau$ is taken as the FWHM of the observed prompt gamma peak in each neutron TOF spectrum. The observed widths of the gamma peaks were 560, 480, 390, and 490 ps FWHM for the 30-, 45-, 60-, and 90-deg detectors, respectively. The calculated energy resolutions were typically 10% at the highest neutron energies observed in a given detector. During preliminary analyses of these data, energy bins as small as 0.25 of the resolution given by Eq. (2) were employed to investigate the effects of the resolution on the shape and structure of the neutron spectra. Since no structure or shape changes were revealed by the fractional binning, the data reported in Sec. IV are binned at a multiple of the resolution in order to increase the statistics in each bin; for ease of presentation, the data are binned at eight times the resolution below 150 MeV and three times the resolution above 150 MeV. The uncertainty δT in the energy associated with the center of each bin is shown in Table I. The uncertainty δT is the result of a one-cm uncertainty in the mean neutron flight path and a one-channel uncertainty in the centroid of the prompt gamma peak relative to the center of each energy bin.

D. Conversion to energy spectra

The prompt-gamma peak in each spectrum provided a reference for calculating absolute neutron flight times. The background-subtracted TOF spectra N, determined by Eq. (1), were converted to energy spectra. The absolute neutron cross sections were calculated from

$$\sigma(\theta,T)=N/[\Omega\epsilon(T)nIm\Delta T]\ . \tag{5}$$

Here N is the number of neutrons in the background-subtracted TOF spectrum from a counter at an angle θ with mean solid angle Ω and efficiency $\epsilon(T)$ in an energy bin of width $m\Delta T$ centered at energy T, where m is a multiple of the energy resolution ΔT. The neutrons were produced in a target of thickness n (nuclei/cm^2) by I incident beam ions. The mean solid angles were calculated from the measured distance between the center of the target and the center of each neutron detector with the exact expression derived by Crawford.[24] The neutron detection efficiency of each counter was calculated with the Monte Carlo code of Cecil *et al.*[18] The calculated efficiencies for the neutron counters in this experiment are listed in Table II; values for neutron energies between the entries in Table II were determined by linear interpolation. The number of beam-telescope coincidences not rejected by the pileup circuit provided the absolute beam normalization I.

E. Summary of uncertainties and corrections

The experimental uncertainties are divided into statistical uncertainties and normalization uncertainties. Table I presents the measured cross sections with their statistical uncertainties $\delta\sigma$. The statistical uncertainties vary from 3—5 % for the low to medium-energy portions of the spectra and increase to about 30% at the highest energies and smallest cross sections measured. The normalization uncertainties are summarized in Table III. The uncertainty in the beam normalization resulting from the pileup circuit was investigated over a wide range of pulse heights and pulse spacings produced by a precision pulse generator. The circuit was observed to reject piled-up pulses with an efficiency of 100%. Since the data-acquisition electronics were gated off during the analysis of a neutron event, there is no dead-time correction to be applied. The resultant uncertainty in the number of accepted neon ions incident on the target is es-

TABLE II. Calculated neutron detection efficiencies.

Energy T (MeV)	Efficiency $N1$ and $N2$ ϵ (%)	$N3$ and $N4$ ϵ (%)
10	7.86	8.26
13	14.1	15.1
16	13.9	14.7
20	13.6	14.2
24	12.6	13.0
28	13.2	13.6
35	14.2	14.9
45	14.9	15.3
60	14.1	14.5
80	12.3	12.2
100	11.4	11.6
130	10.3	10.4
160	10.1	10.5
200	9.99	10.4
300	10.0	10.2
500	10.2	10.3
800	9.83	10.3

TABLE III. Summary of normalization uncertainties.

Source	Uncertainty (%)
Incident ions	1
Solid angle	1
Flight path	2
Efficiency	5—10[a]
Target thickness	3
Target attenuation	2
Air attenuation	2
	8—12

[a]The uncertainty in the efficiency is estimated to be about 5% above 18 MeV and increases to 10% at 12 MeV.

timated to be less than 1%. The uncertainty in the mean solid angle is less than 1%; it is dominated by the uncertainty in the flight path of a detected neutron in the 10 cm thickness of the neutron counter. The uncertainty in the calculated efficiencies, for a well-known threshold, is estimated by Cecil *et al.*[18] to be about 4% by comparison with several measurements of neutron detector efficiencies. Uncertainties in the pulse-height calibration of the neutron detectors produce uncertainties in the threshold settings and result in an additional uncertainty in the efficiencies which decrease from about 10% at 12 MeV to about 5% at energies greater than 18 MeV. The uncertainty in the measurement of the target thickness is estimated to be about 3%. Neutron attenuation in the target was investigated with two thicknesses (1.86 and 5.60 g/cm^2) of uranium. The cross sections measured with each of the targets were systematically the same within statistics, which were typically 5% per energy bin; in addition, smooth curves drawn through the spectra from the two targets were observed to be the same within 2% or better. The attenuation in the target calculated for a mean-free path of 180 g/cm^2 is 2% for neutrons emitted at 30 deg and 3% for neutrons emitted at 90 deg. The neutron attenuation in the air is negligible in comparison with that in the target. No correction for target or air attenuation is indicated. The total scale uncertainty, taken as the Gaussian quadrature sum of the individual scale uncertainties, is about 8% for neutron energies above 18 MeV and increases to about 12% at 12 MeV.

IV. NEUTRON SPECTRA

Presented in Table I are the inclusive doubly differential cross sections for the production of neutrons at laboratory angles of 30, 45, 60, and 90 deg by 337 MeV/nucleon neon ions reacting in targets of carbon, aluminum, copper, and uranium. The spectra start at neutron energies of about 12 MeV and extend to the highest neutron energies observed at each angle. The energy associated with each laboratory cross section is the mean energy of an energy bin which extends halfway to each of the nearest neighboring energies. The neutron spectra for the carbon, aluminum, copper, and uranium targets are plotted in Figs. 4—7, respectively.

Presented in Table IV for each of the targets are the integrated cross sections above 25 MeV, which exclude almost all of the neutron evaporation. The cross sections integrated over all measured neutron energies above 25 MeV were fit well by a simple exponential decreasing with increasing angle. The fitted exponential was integrated over angle to obtain the measured 30 to 90 deg total cross section. The total cross sections for the angular regions from 0 to 30 deg and from 90 to 180 deg were estimated by extrapolating the exponential fit. The measured 30 to 90 deg total cross sections have an

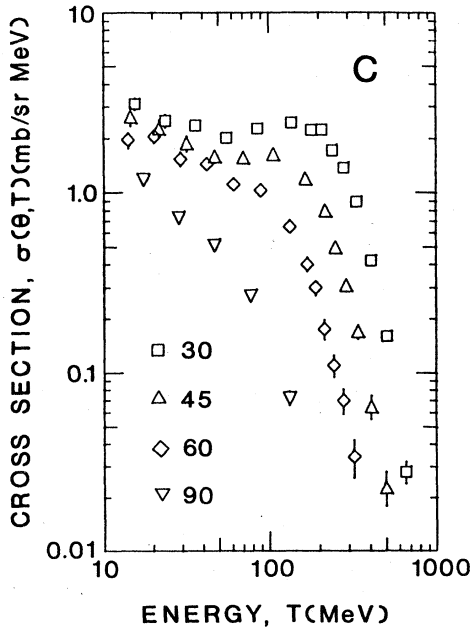

FIG. 4. Neutron double-differential cross section at angles of 30, 45, 60, and 90 deg versus neutron energy for 337 MeV/nucleon neon ions on a carbon target.

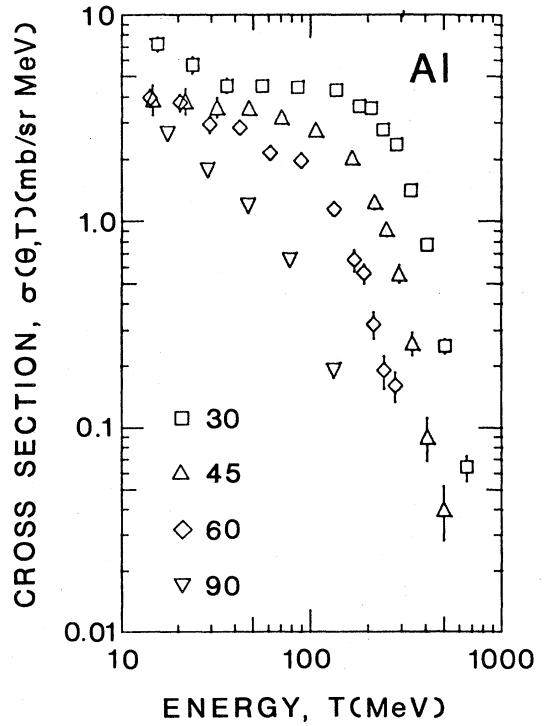

FIG. 5. Neutron double-differential cross section at angles of 30, 45, 60, and 90 deg versus neutron energy for 337 MeV/nucleon neon ions on an aluminum target.

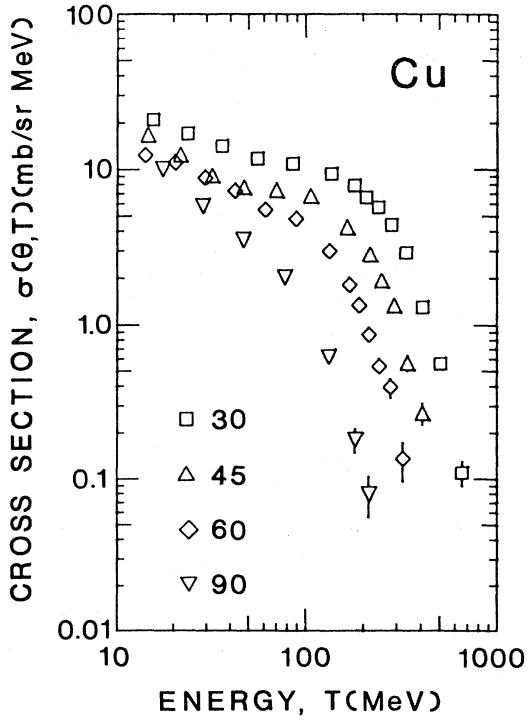

FIG. 6. Neutron double-differential cross section at angles of 30, 45, 60, and 90 deg versus neutron energy for 337 MeV/nucleon neon ions on a copper target.

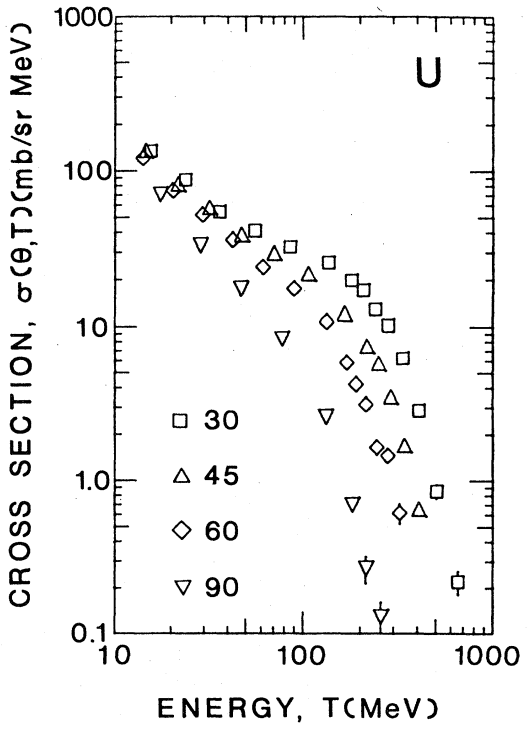

FIG. 7. Neutron double-differential cross section at angles of 30, 45, 60, and 90 deg versus neutron energy for 337 MeV/nucleon neon ions on a uranium target.

absolute uncertainty of about 10%. The 30 to 90 deg region typically contains more than half of the total neutron production. The estimated production in the 0 to 30 deg region is always three or more times larger than the estimated production in the 90 to 180 deg region. Also listed in Table IV are the neutron multiplicities obtained by dividing the total integrated cross sections by the geometric reaction cross section of the appropriate projectile-target system.

Three different energy regions can be distinguished in the neutron spectra: (1) a low-energy "evaporation" region, (2) a high-energy exponential tail reflecting the internal momentum distribution of the nucleons, and (3) an intermediate-energy region reflecting quasifree and preequilibrium processes. The intermediate-energy region becomes less pronounced with increasing angle and is almost nonexistent at 90°. This behavior is consistent with the interpretation that the intermediate-energy region consists mainly of scattering processes with a few impulsive direct collisions. The intermediate-energy region is relatively flat at the forward angles and merges into an

TABLE IV. Total energy and angle integrated neutron cross sections above 25 MeV produced by 337 MeV/nucleon neon ions in targets of uranium, copper, aluminum, and carbon. The estimated uncertainty of the measured 30 to 90 deg total cross sections is about 10%.

Target	Cross section $\sigma(T>25$ MeV) (barns) Estimated (0–30 deg)	Measured (30–90 deg)	Estimated (90–180 deg)	Total	Neutron multiplicity
Uranium	9.20	17.10	3.20	29.50	8.3
Copper	3.39	4.59	0.52	8.50	4.2
Aluminum	1.60	1.80	0.15	3.55	2.4
Carbon	1.09	1.03	0.06	2.18	1.9

exponential falloff at wide angles. The 30-deg spectrum from the carbon target shows a broad peak around 150 MeV, which we interpret as a signature of quasifree nucleon-nucleon collisions. It is reasonable to expect this signature from the lighter system because the smaller number of participating particles is less likely to wash out the kinematic relationships for quasifree nucleon-nucleon collisions. Although the neutron detection threshold does not permit us to see the evaporation peaks, we do see evidence of the evaporation tails. The evaporation yields apparent in our spectra increase with the mass number of the target. The cross sections at low energies increase with decreasing energy for all of the targets; for the uranium target, this increase is most rapid and the angular distribution of the low-energy neutrons approaches isotropy. These general features of the spectra are consistent with the picture that the reactions start with individual collisions between nucleons in the projectile and target. The reaction products from these interactions are forward peaked and produce a shoulder observed at 30 deg in the light-target spectra between 100 and 200 MeV. For the heavy targets, the products of the initial nucleon-nucleon interactions are less likely to escape the target nucleus without further interacting; thus, the direct-reaction peak is reduced severely. The increased number of interactions for heavy targets is responsible also for the increased yields of low-energy neutrons. The nearly isotropic distribution of the lowest energy neutrons from the uranium target is consistent with the neutron emission expected from a system in thermal equilibrium.

The neutron cross sections calculated with the thermodynamic firestreak model[9,10] of heavy-ion reactions are compared in Figs. 8 and 9 with our measurements at angles of 30 and 90 deg, respectively. The curves represent the firestreak cross sections for 337 MeV/nucleon neon ions on the uranium and carbon targets. The firestreak cross sections exhibit the high-energy exponential tail, which decreases exponentially with increasing neutron energy. This decrease results from the decay of the thermal equilibrium assumed by the fire-

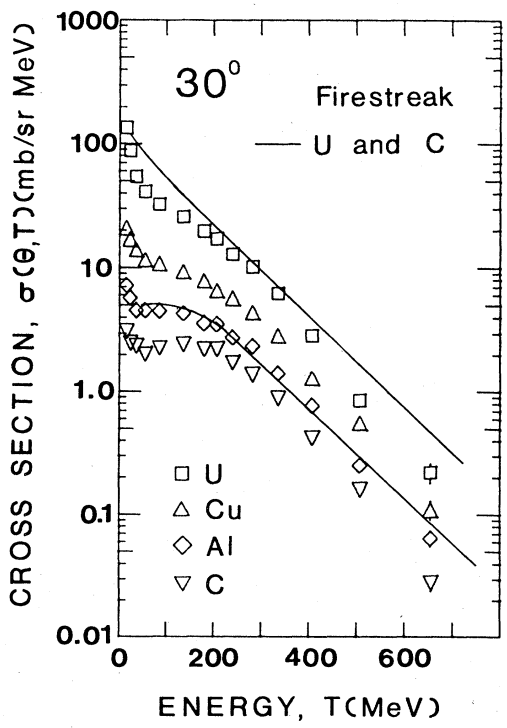

FIG. 8. Neutron double-differential cross sections at 30 deg for 337 MeV/nucleon neon ions on targets of uranium, copper, aluminum, and carbon compared with calculations of the firestreak model for targets of uranium (upper line) and aluminum (lower line).

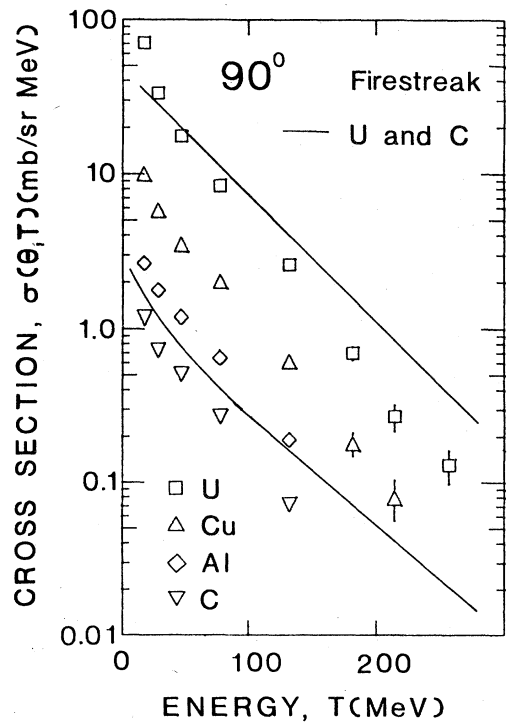

FIG. 9. Neutron double-differential cross sections at 90 deg for 337 MeV/nucleon neon ions on targets of uranium, copper, aluminum, and carbon compared with calculations of the firestreak model for targets of uranium (upper line) and aluminum (lower line).

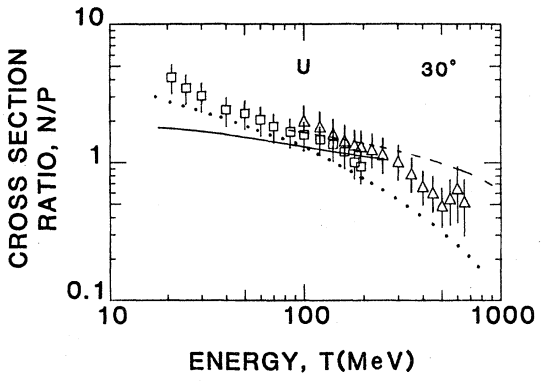

FIG. 10. Emitted neutron-to-proton cross section ratios at 30 deg for a uranium target. The squares are ratios of the neutron measurements at 337 MeV/nucleon to the proton measurements of Sandoval *et al.* (Ref. 2) at 393 MeV/nucleon; the triangles are ratios for the proton measurements of Nagamiya *et al.* (Ref. 4) for a lead target at 385 MeV/nucleon. The solid, dashed, and dotted lines are the results of calculations discussed in the text.

streak model to occur in the overlapping regions of the target and projectile. The fact that the firestreak cross sections do not decrease as rapidly as the data at both 30 and 90 deg indicates a lower-temperature thermal-decay process or a semidirect scattering mechanism. The firestreak cross sections are consistently larger than the measured values except at the lowest energies, where the tails of the evaporation peaks evident in the data increase rapidly to become comparable to the calculations. The overestimate of the firestreak cross sections may be due to the omission of nuclear transparency in the calculations presented here. The discrepancy in magnitude between the firestreak cross sections and the data above about 100 MeV is significant. Note that composite-particle production is small compared to the nucleon production at these energies.

V. NEUTRON-TO-PROTON CROSS SECTION RATIOS

Emitted neutron-to-proton (n/p) cross section ratios at 30 and 90 deg are presented in Figs. 10—15 for uranium, copper, and aluminum calculated from the neutron data and the available proton data.[2,4] The n/p ratios calculated with the proton data of Sandoval *et al.*[2] are shown as squares. The n/p ratios calculated with the proton data of Nagamiya *et al.*[4] are shown as triangles. The error bars are the Gaussian-quadrature sum of the neutron and proton statistical uncertainties plus the uncertainties in the normalizations of the neutron and proton measurements. The uncertainty in the normalization of the neutron data is about 10%. The normalization uncertainty for each of the proton measurements is 20%. The uncertainty in the energy of each point in Figs. 10—15 for the n/p ratios is a combination of the uncertainties in the neutron and proton cross section energy calibrations and is always smaller than the width of the symbols. The neutron energy uncertainty δT is 2% as given in Table I. The uncertainty in the momentum calibration of the proton measurements is several percent.

In Figs. 10 and 11, we plot the n/p ratios calculated with the neutron data from a uranium target and the proton data of Sandoval *et al.* from a uranium target (squares) and the proton data of Nagamiya *et al.* from a lead target (triangles). For energies greater than about 30 MeV, the two sets of proton data are expected to differ by the ra-

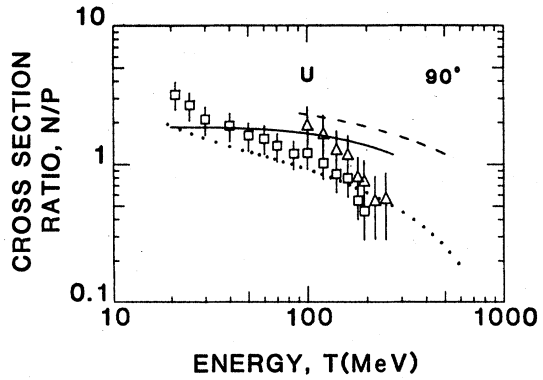

FIG. 11. Emitted neutron-to-proton cross section ratios at 90 deg for a uranium target. The squares are ratios of the neutron measurements at 337 MeV/nucleon to the proton measurements of Sandoval *et al.* (Ref. 2) at 393 MeV/nucleon; the triangles are ratios for the proton measurements of Nagamiya *et al.* (Ref. 4) for a lead target at 385 MeV/nucleon. The solid, dashed, and dotted lines are the results of calculations discussed in the text.

tio of the uranium-to-lead proton numbers of about 12%. Below about 30 MeV, neutrons from fission products may be present in the uranium spectrum but not in the lead spectrum. Between 100 and 200 MeV, the proton measurements and their resulting n/p ratios differ by 30—50 %, but normalization and statistical uncertainties make it difficult to determine if this difference is significant. Shown in Figs. 12 and 13 are the n/p ratios from copper.

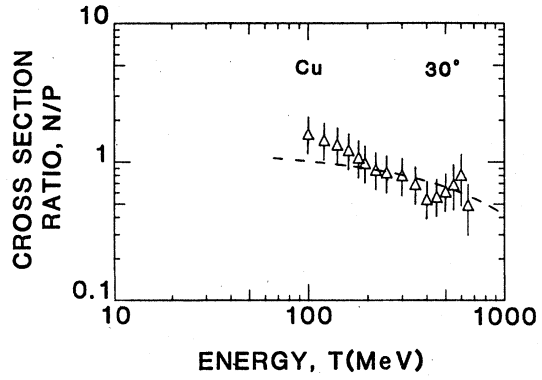

FIG. 12. Emitted neutron-to-proton cross section ratios at 30 deg for a copper target. The triangles are the ratios of the neutron measurements at 337 MeV/nucleon to the proton measurements of Nagamiya *et al.* (Ref. 4) at 385 MeV/nucleon. The dashed line is discussed in the text.

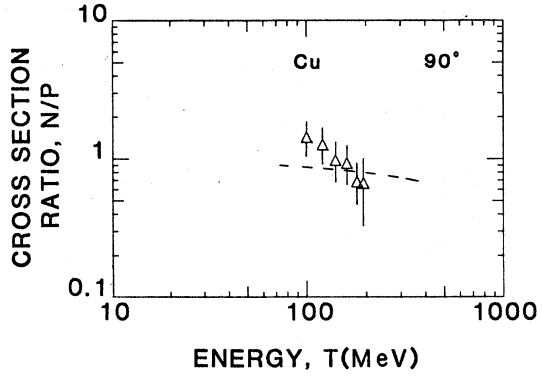

FIG. 13. Emitted neutron-to-proton cross section ratios at 90 deg for a copper target. The triangles are the ratios of the neutron measurements at 337 MeV/nucleon to the proton measurements of Nagamiya *et al.* (Ref. 4) at 385 MeV/nucleon. The dashed line is discussed in the text.

The proton measurements from a copper target are those of Nagamiya *et al.* In Figs. 14 and 15, we show the n/p ratios calculated from the neutron data for an aluminum target and the proton data of Sandoval *et al.* for an aluminum target (squares) and the proton data of Nagamiya *et al.* for a sodium-fluoride target (triangles). The expected difference between the proton measurements caused by the difference in target proton numbers is about 12%. The 30 deg n/p ratios calculated from the

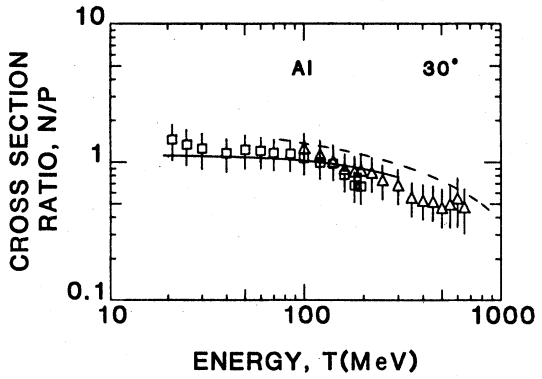

FIG. 14. Emitted neutron-to-proton cross section ratios at 30 deg for an aluminum target. The squares are ratios of the neutron measurements at 337 MeV/nucleon to the proton measurements of Sandoval *et al.* (Ref. 2) at 393 MeV/nucleon; the triangles are ratios for the proton measurements of Nagamiya *et al.* (Ref. 4) at 385 MeV/nucleon. The solid and dashed lines are discussed in the text.

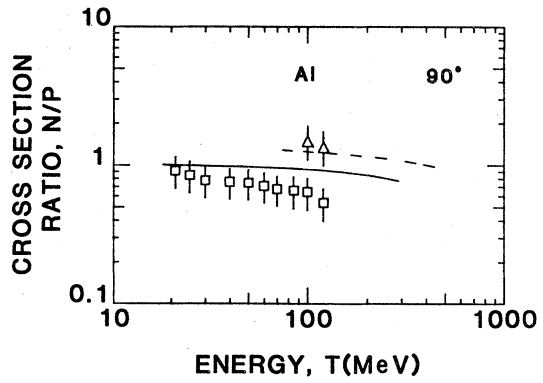

FIG. 15. Emitted neutron-to-proton cross section ratios at 90 deg for an aluminum target. The squares are ratios of the neutron measurements at 337 MeV/nucleon to the proton measurements of Sandoval *et al.* (Ref. 2) at 393 MeV/nucleon; the triangles are ratios for the proton measurements of Nagamiya *et al.* (Ref. 4) at 385 MeV/nucleon. The solid and dashed lines are discussed in the text.

two sets of proton data are about the same within the associated uncertainties. The sodium-fluoride ratios tend to be slightly larger than the aluminum ratios as expected from the ratio of the target proton numbers. The 90 deg n/p ratios calculated from the two sets of proton data differ by about a factor of 2.

Comparisons of the n/p ratios in Figs. 10–15 are nearly independent of the target nucleus at the higher energies. For each of the three targets, the high-energy tails of the 30 deg n/p ratios decrease to 0.5 at about 500 MeV. The 90 deg ratios decrease to 0.5 near 200 MeV. Below 100 MeV the 30 deg uranium n/p ratios increase to about 2.5 at 40 MeV and about 3.5 near 20 MeV where fission products may be significant. The 90 deg n/p ratios increase to about 1.7 at 40 MeV and to about 2.2 near 20 MeV. There are no proton cross sections for copper below about 100 MeV. The 30 deg aluminum n/p ratios between 20 and 100 MeV are nearly flat and are typically about 1.3. The 90 deg ratios increase slowly below 100 MeV and reach a value of about 0.8 near 20 MeV.

Quantitative comparison of the n/p ratios with models of relativistic heavy-ion reactions is complicated by the difference in incident neon-ion beam energies. The proton measurements of Sandoval *et al.* and Nagamiya *et al.* were made with neon beam energies of 393 and 385 MeV/nucleon, respectively, whereas the mean beam energy was 337 MeV/nucleon for the neutron measurements.

Schimmerling *et al.*[7] showed that the neutron and proton spectra calculated at the appropriate beam energies with the thermodynamic firestreak model[8] do not reproduce the experimental heavy target n/p ratios. These firestreak calculations are shown in Figs. 10 and 11. The solid line shows the result of the firestreak calculations for the ratio (Ne+U$\rightarrow n+X$ at 337 MeV/nucleon)/(Ne + U $\rightarrow p+X$ at 393 MeV/nucleon). The dashed line shows the result of the firestreak calculations for the ratio (Ne + U $\rightarrow n+X$ at 337 MeV/nucleon)/(Ne + Pb $\rightarrow p+X$ at 385 MeV/nucleon). At high energies, the experimental n/p ratios decrease much more rapidly than the firestreak calculations. Below about 100 MeV, the firestreak calculations increase much less rapidly than the experimental n/p ratios.

In Figs. 12 and 13, we present the result of the firestreak calculations (dashed line) for the ratio (Ne + Cu $\rightarrow n+X$ at 337 MeV/nucleon)/(Ne + Cu $\rightarrow p+X$ at 385 MeV/nucleon). At both 30 and 90 deg, the experimental n/p ratios decrease at high energies more rapidly than the firestreak calculations. The solid lines in Figs. 14 and 15 show the result of the firestreak calculations for the ratio (Ne + Al $\rightarrow n+X$ at 337 MeV/nucleon)/(Ne + Al $\rightarrow p+X$ at 393 MeV/nucleon). The dashed lines in Figs. 14 and 15 show the result of the firestreak calculations for the ratio (Ne + Al $\rightarrow p+X$ at 337 MeV/nucleon)/(Ne + NaF $\rightarrow p+X$ at 385 MeV/nucleon). The 30 deg firestreak calculations reproduce the experimental n/p ratios below about 150 MeV, but it should be noted that the neutron and proton cross sections calculated by the firestreak model are both larger than the experimental data by about a factor of 2. At energies greater than 200 MeV, the experimental n/p ratios decrease more rapidly than the firestreak calculations. At 90 deg, the firestreak calculations are nearly flat between 20 and 200 MeV. The experimental n/p ratios decrease significantly with increasing energy.

Gyulassy and Kauffman[16] investigated the effects of the nuclear Coulomb potential on the uranium n/p ratios. Their calculation, which is based on thermodynamic considerations similar to those of the fireball and firestreak models, is shown as a dotted line in Figs. 10 and 11. This calculation reproduces the shapes of the 30 and 90 deg n/p ratios significantly better than the firestreak model, which does not include any Coulomb effects. The Coulomb effects for the copper and aluminum targets are expected to be significantly less than those

for the uranium target and cannot alone account for the observed rapid decrease in the experimental n/p ratios at high energies; however, the Coulomb effects may be important to describe nucleon spectra emitted in collisions with high Z targets and/or projectiles.

Stevenson[15,17] used a relativistic cascade model to calculate n/p ratios for a uranium target directly from the cross sections for production of protons, neutrons, and light nuclei without introducing any parameters. He compared the calculated "primordial" or precoalescence n/p ratios with the primordial spectra ratios which he determined from the measurements of proton, neutron, and composite particle spectra. The primordial cross sections were determined from experiment by Eqs. (6) and (7):

$$\left[\frac{d^2\sigma}{d\Omega dT}\right]_{\text{primordial}} = \sum_{\text{all isotopes}} Z\frac{d^2\sigma_{\text{exp}}(Z,A)}{d\Omega\, dT} \quad \text{(for protons)}, \tag{6}$$

$$\left[\frac{d^2\sigma}{d\Omega\, dT}\right]_{\text{primordial}} = \sum_{\text{all isotopes}} (A-Z)\frac{d^2\sigma_{\text{exp}}(Z,A)}{d\Omega\, dT} \quad \text{(for neutrons)}. \tag{7}$$

The primordial proton spectrum is seen to be just the sum of the proton cross section and all the emitted composite particle cross sections weighted by the number of protons in the composite particle. Similarly, the primordial neutron spectrum is the sum of the neutron cross section and all the composite particle cross sections weighted by the number of neutrons in the composite particle. The calculation of the primordial spectra in this fashion assumes that the observed composite particle of energy $T\cdot A$ prior to coalescence forms from A nucleons each of energy T.

The primordial n/p ratios in Stevenson's cascade model are determined primarily by the n/p ratio of the target and projectile. For neutron and proton measurements made with a 400 MeV/nucleon neon projectile and a uranium target, the cascade model predicts that (1) the n/p ratio at low energies approaches that of the target alone, and (2) the n/p ratio at high energies approaches that of the projectile alone. This same prediction is made by the firestreak model; however, the neutron and proton cross sections calculated from the firestreak model decrease much less rapidly at high energies than either the measured cross sections or those obtained from Stevenson's cascade model. Stevenson concludes that the rapid decrease of the experimental n/p ratios at high energies is primarily the result of the different beam energies of the neutron and proton measurements. Stevenson's[15,17] cascade model reproduces the primordial neutron and proton production cross sections from a uranium target to within about 20% at both 30 and 90 deg. The n/p ratios calculated by his cascade model reproduce the experimental n/p ratios for uranium within the accuracy of the experimental measurements. The failure of the firestreak model to reproduce the experimental n/p ratios is probably the result of the assumption of thermal equilibrium of the firestreak. The validity of this assumption was investigated by Stevenson with his cascade model.[15] He estimates that the average number of scatterings of an emitted nucleon in a neon or uranium interaction is about five, but that about 13% scatter only once. Thus, although some of the nucleons may reach a thermal equilibrium after 5 or more scatters, there is a significant nucleon component which scatters only once or twice prior to emission. The fact that this component changes more rapidly with beam energy than does the thermal equilibrium of the firestreak probably accounts for the improved agreement of Stevenson's cascade model with the experimental n/p ratios.

V. CONCLUSIONS

We measured inclusive double-differential cross sections at angles of 30, 45, 60, and 90 deg for the production of neutrons above about 12 MeV from 337 MeV/nucleon neon ions bombarding targets of C, Al, Cu, and U. We compared these cross sections with predictions of two models of emitted nucleon spectra from relativistic heavy-ion reactions. The "firestreak" thermodynamic model does not reproduce the high-energy tails of the observed cross sections from targets of uranium, copper, and aluminum; furthermore, firestreak calculations for these same targets performed at the beam energies corresponding to the neutron and proton measurements do not reproduce the rapid decrease of the experimentally observed n/p ratios above 200 MeV. The failure of the firestreak model to repro-

duce these characteristics of the measured spectra occurs probably because of the assumption of thermodynamic equilibrium for the reactions. Some of the discrepancy may result from the omission of final-state Coulomb effects in the model. The predictions of the intranuclear-cascade model of Stevenson, which are reported only for a uranium target, reproduce the observed n/p ratios and the high-energy tails of the nucleon cross sections fairly well. Stevenson concludes that the rapid decrease of the n/p ratios above 200 MeV results primarily from the difference in the beam energies of the neutron and proton measurements. Planned experiments to measure neutron spectra at the same beam-energy of the proton spectra measurements should elucidate this point.

The results presented here extend our earlier results reported only for a uranium target to lighter-mass targets. The measurements from the different targets indicate that three different energy regions can be identified in the neutron spectra. The low-energy evaporation region increases dramatically with increasing target mass, and becomes nearly isotropic for the uranium target. The high-energy tail of each spectrum is fit well by a decreasing exponential and reflects the internal momentum distribution of the target and projectile nucleons. Finally, there is an intermediate-energy region which exhibits a characteristic quasifree peak somewhat below the projectile beam energy per nucleon at forward angles in the light targets. This quasifree peak becomes almost nonexistent for the heavier targets. The general features of the neutron spectra are consistent with the idea that the reactions start with individual, quasifree collisions between nucleons and then proceed toward equilibrium in subsequent interactions.

ACKNOWLEDGMENTS

This work was supported in part by the U.S. National Science Foundation, the U.S. Department of Energy, and the National Aeronautics and Space Administration. We are grateful to Gary Westfall for providing a copy of the firestreak computer code, and to S. Nagamiya for proton cross sections prior to publication. We acknowledge useful conversations with M. Gyulassy regarding final-state Coulomb effects and K. Crebbin regarding Bevalac beam energy calibrations.

---

*Present Address: Varian Associates, Palo Alto, California 94303.

†Present Address: UCSF - RIL, South San Francisco, California 94080.

[1]J. Gosset, H. H. Gutbrod, W. G. Meyer, A. M. Poskanzer, A. Sandoval, R. Stock, and G. D. Westfall, Phys. Rev. C 16, 629 (1977).

[2]A. Sandoval, H. H. Gutbrod, W. G. Meyer, R. Stock, Ch. Lukner, A. M. Poskanzer, J. Gosset, J. C. Jourdoin, C. H. King, G. King, Nguyen Van Sen, G. D. Westfall, and K. L. Wolf, Phys. Rev. C 21, 1321 (1980).

[3]M. M. Gazzaly, J. B. Carroll, J. V. Geaga, G. Igo, J. B. McClelland, M. A. Nasser, H. Spinka, A. L. Sagle, V. Perez-Mendez, R. Talaga, E. T. B. Wipple, and F. Zarbakhsh, Phys. Lett. 79B, 325 (1978).

[4]S. Nagamiya, M. -C. Lemaire, E. Moeller, S. Schnetzer, G. Shapiro, H. Steiner, and I. Tanihata, Lawrence Berkeley Laboratory Report No. LBL-12123, 1981; E. Moeller, M. -C. Lemaire, S. Nagamiya, S. Schnetzer, H. Steiner, and I. Tanihata, Lawrence Berkeley Laboratory Report No. LBL-12257, 1981.

[5]R. Nakai, J. Chiba, I. Tanihata, S. Nagamiya, H. Bowman, J. Ioannou, and J. O. Rasmussen, in *Proceedings of the International Conference on Nuclear Structure, Tokyo, 1977* (International Academic Printing Co., Ltd., Tokyo, 1977).

[6]H. H. Gutbrod, A. Sandoval, P. J. Johansen, A. M. Poskanzer, J. Gosset, W. G. Meyer, G. D. Westfall, and R. Stock. Phys. Rev. Lett. 37, 667 (1976).

[7]W. Schimmerling, J. W. Kast, D. Ortendahl, R. Madey, R. A. Cecil, B. D. Anderson, and A. R. Baldwin, Phys. Rev. Lett. 43, 1985 (1979).

[8]G. D. Westfall, J. Gosset, P. J. Johansen, A. M. Poskanzer, W. G. Meyer, H. H. Gutbrod, A. Sandoval, and R. Stock. Phys. Rev. Lett. 37, 1202 (1976).

[9]W. D. Myers, Nucl. Phys. A296, 177 (1978).

[10]J. Gosset, J. I. Kapusta, and G. D. Westfall, Phys. Rev. C 18, 844 (1978).

[11]A. A. Amsden, J. N. Ginocchio, F. B. Harlow, J. R. Nix, M. Danos, E. C. Halbert, and R. K. Smith, Phys. Rev. Lett. 38, 1055 (1977).

[12]A. A. Amsden, F. H. Harlow, and J. R. Nix, Phys. Rev. C 15, 2059 (1977).

[13]Y. Yariv and Z. Fraenkel, Phys. Rev. C 20, 2227 (1979).

[14]J. Bondorf, H. T. Feldmeier, S. Garpman, and E. C. Halbert, Phys. Lett. 65B, 217 (1976).

[15]J. D. Stevenson, Phys. Rev. Lett. 41, 1702 (1978).

[16]M. Gyulassy and S. K. Kauffman, Lawrence Berkeley Laboratory Report No. LBL-10279, 1980.
[17]J. D. Stevenson, Phys. Rev. Lett. 45, 1773 (1980).
[18]R. A. Cecil, B. D. Anderson, and R. Madey, Nucl. Instrum. Methods 161, 439, 1979.
[19]Q. Kerns, IEEE Trans. Nucl. Sci. 24, 353 (1977).
[20]H. W. Patterson and R. H. Thomas, *Accelerator Health Physics* (Academic, New York, 1973).
[21]A. R. Baldwin and R. Madey, Nucl. Instrum. Methods 171, 149 (1980).
[22]G. Gabor, private communication.
[23]H. Knox and T. Miller, Nucl. Instrum. Methods 101, 519 (1972).
[24]F. S. Crawford, Rev. Sci. Instrum. 24, 552 (1953).